AIAA SciTech Forum
6-10 January 2025, Orlando, FL
AIAA SCITECH 2025 Forum

10.2514/6.2025-1099.c1

Correction: Comparison of the Near-Field Electron Properties of a Magnetically-shielded Hall Effect Thruster in Various Electrical Configurations

Author(s) Name: Naia Butler-Craig, Julian Lopez-Uricoechea, Dan Lev, Mitchell L. R. Walker, Jean Luis Suazo Betancourt
Author(s) Affiliations: For authors 1-4 Georgia Institute of Technology, Atlanta, Georgia, 30332, United States of America. For author 5 The Aerospace Corporation, Arlington, VA, 22202, United States of America

Correction Notice

The authors would like to acknowledge Janice Cabrera in the acknowledgements section of the article for her contributions to data collection used in Figure 7b.

Downloaded by 2600:6c5a:5af0:68f0:7830:8957:b162:4697 on February 10, 2025 | http://arc.aiaa.org | DOI: 10.2514/6.2025-1099.c1

Copyright © 2025 by the American Institute of Aeronautics and Astronautics, Inc. All rights reserved.

AIAA SciTech Forum
6-10 January 2025, Orlando, FL
AIAA SCITECH 2025 Forum

10.2514/6.2025-1099

Comparison of the Near-Field Electron Properties of a Magnetically-shielded Hall Effect Thruster in Various Electrical Configurations

Naia Butler-Craig[1],
Georgia Institute of Technology, Atlanta, Georgia, 30332, United States of America

Jean Luis Suazo Betancourt[2]
The Aerospace Corporation, Arlington, VA, 22202, United States of America

Julian Lopez-Uricoechea[3], Dan Lev[4], Mitchell L. R. Walker[5]
Georgia Institute of Technology, Atlanta, Georgia, 30332, United States of America

Downloaded by Georgia Institute of Technology (Georgia Tech) on January 17, 2025 | http://arc.aiaa.org | DOI: 10.2514/6.2025-1099

Abstract

Due to the lack of physics-based predictive modeling of HET operation, ground-based facility effects on thruster operation make it difficult to predict the on-orbit performance. The goal of the electric propulsion community is to accurately extrapolate thruster performance on the ground to the space environment. Yet, the electrical configuration of the HET is an important consideration in efforts to characterize the ground-based performance of the HET. In this study, laser Thomson scattering (LTS) is used to measure the near field, axially resolved electron properties 1 to 17.75 mm downstream of the center-mounted cathode, which is flush with the thruster's exit plane. The measurements were taken in the H9 HET at its nominal 300 V, 6-kW operating condition in three different electrical configurations: thruster body floating, cathode tied to thruster body, and thruster body grounded. The experiments were performed in Vacuum Test Facility -2 at the Georgia Tech High-power Electric Propulsion Laboratory at an operation pressure of 8 μTorr-Kr. The cathode-tied electrical configuration consistently had the greatest electron density from 1 to 13 mm downstream of the cathode. The cathode-tied configuration at one position produced an electron number density more than 40% higher than the other configurations. From 13 to 17.75 mm downstream of the cathode, the electron density was approximately equal for all three electrical configurations. The electron temperature in the grounded condition was the lowest, 13% lower than the floating configuration, at all positions where the cathode tied and thruster body floating conditions remained virtually equal.

I. Nomenclature

A = amplitude of oscillation
A_s = surface area
b_J = Placzek-Teller coefficient
B_g = rotational energy constant
D_g = centrifugal distortion constant

---

[1] Graduate Research Assistant, School of Aerospace Engineering, and AIAA Student Member; naiabc3@gatech.edu.
[2] Technical Staff, System Concepts Optimization, and AIAA Member; jlsb3@gatech.edu.
[3] Graduate Research Assistant, School of Aerospace Engineering, and AIAA Student Member; jlopezur3@gatech.edu.
[4] Research Engineer, School of Aerospace Engineering, and AIAA Associate Fellow; dan.lev@gatech.edu.
[5] Professor and Chair, School of Aerospace Engineering, and AIAA Fellow; mitchell.walker@ae.gatech.edu.

Copyright © 2025 by the American Institute of Aeronautics and Astronautics, Inc. All rights reserved.

$\Delta\emptyset$ = potential difference
c = speed of light
c_p = pressure coefficient
e = elementary charge
η = intensified photoelectron
ϵ_J = energy mode
E_i = incident laser energy
f_i = breathing mode frequency
g_J = degeneracy
h = Planck’s constant
I_e = electron current
I_i = ion current
I_g = nuclear spin quantum number
J = energy level
k_B = Boltzmann constant
λ_i = incident wavelength
$\lambda_{J'}$ = Raman shifted wavelength
L = length of probe volume
$L_{\mathrm{ion/accel}}$ = ionization/acceleration region length
m_i = ion mass
m_e = electron mass
n_g = gas number density
n_o = local plasma density
n_J = population in J
$\Delta\Omega$ = solid angle of collection
φ_f = floating potential
p_g = gas pressure
P_λ^R = Raman scattering signal
P_λ^T = Thomson scattering signal
Q_g = rotational partition function
ρ = depolarization ratio
σ_{IF} = instrument function
T_e = electron temperature
T_g = gas temperature
τ = full-width half maximum
θ_{kio} = angle between incident radiation propagation direction and scattering observation
θ_{eiz} = angle between incident radiation polarization and z axis
v_{ion} = ion velocity
v_n = neutral velocity
ζ = polarization angle between incident and scattered radiation
$\frac{\partial\sigma^R}{\partial\Omega}$ = Raman scattering cross section
$\frac{\gamma^2}{{\epsilon_o}^2}$ = anisotropy of molecular polarizability tensor

II. Introduction

Hall effect thrusters (HETs) are a cornerstone of modern electric propulsion systems, widely utilized in both commercial and scientific space missions because of their high specific impulse of over 1,000 s, high thrust-to-power ratio, and high reliability [1]. Magnetically-shielded HET’s utilize a transverse magnetic field to trap electrons, creating a high-density plasma region at the thruster exit plane. In this region, the high temperature, >20 eV, electrons ionize the propellant gas while an applied electric field accelerates the ions through the thruster's exit [2]. The resulting ion beam generates thrust, while the electrons neutralize the ion beam to maintain plasma plume charge neutrality. This method offers high efficiency and exit velocity, making HETs ideal for long-duration space missions and satellite

Downloaded by Georgia Institute of Technology (Georgia Tech) on January 17, 2025 | http://arc.aiaa.org | DOI: 10.2514/6.2025-1099

Downloaded by Georgia Institute of Technology (Georgia Tech) on January 17, 2025 | http://arc.aiaa.org | DOI: 10.2514/6.2025-1099

station-keeping. Various institutions have sought to optimize and increase their suitability for said mission applications through several design considerations, including but not limited to magnetic field optimization, *e.g.*, magnetic shielding, [3], flight-like ground-based testing environments, and simulations that allow ground testing results to be accurately extrapolated to performance in space.

Understanding and mitigating facility interaction is crucial as this technology continues to develop for more rigorous mission applications. These interactions yield information about how the thruster will not only perform in space but also interact with the spacecraft. Studies in the last decade have identified a facility interaction, outside of the thoroughly investigated elevated pressure effects, that involves the electrical interaction of the conducting vacuum facility with the HET plume [4-5]. The electrical configuration of the thruster, or how the thruster electrodes and chassis are connected, plays a major role in this. Peterson *et al.* in Ref. [6] completed detailed performance maps of NASA's 12.5-kW Hall Effect Rocket with Magnetic Shielding (HERMeS) Technology Demonstration Unit-1 (TDU-1) with the thruster in several ground-based electrical configurations. The study aimed to assess the best electrical configuration to conduct development and qualification testing for flight missions. An additional facet of the study was varying the exit plane boundary condition between a dielectric and conducting surface. This was employed using dielectric and conducting pole covers. While grounding the thruster body by electrically connecting it to the conducting vacuum chamber yielded the highest performance in this study, this configuration was not ideal since it created a low-resistance electron pathway through the conducting chamber, allowing electrons to recombine with plume ions at the chamber walls—a condition not representative of the space environment [5]. Peterson *et al.* confirmed this with a measurement of 10% of the discharge current flowing through the thruster body to ground in this configuration [6]. Another electrical configuration for the HET is isolating the thruster body from the vacuum chamber and allowing it to float electrically. This configuration was employed by HETs in flight on the ESA SMART-1 spacecraft [7]. However, in space, the thruster was electrically connected to the spacecraft, which also floated relative to the local plasma potential. While the floating configuration is more representative of the flight environment for ground-based testing, it does result in very negative floating potentials of the thruster body [8]. The resultant plasma sheaths accelerate ions toward components at the thruster body potential. These ions increase the erosion of the plasma-facing thruster components at the thruster body potential. The final configuration examined by the author was electrically connecting the thruster body to the cathode common to limit the floating potential of the thruster body, thus mitigating possible erosion due to energetic ions [9]. It was found that this configuration provided negligible decay in performance from the grounded configuration while still being representative of the flight environment. The power spectral density (PSD) plots performed in the study showed variance in the discharge current oscillation current characteristics that may influence the near-field thruster plume physics [10]; however, no near-field measurements were taken. It has been postulated and measured by authors in Ref. [11] that the electrons collected by the plasma-facing thruster components are conducted and re-emitted through the cathode. These parameters have not been definitively measured. Understanding the electron properties in the near field of HETs, immediately adjacent to the thruster exit plane, is difficult because the environment consists of complex plasma phenomena that significantly influence thruster operation.

The primary objective of this study is to characterize and understand how the near-field plasma properties, electron temperature and electron density, change downstream of the cathode centerline in each electrical configuration. An incoherent laser Thomson scattering (LTS) diagnostic is employed to make these measurements. LTS is a noninvasive diagnostic technique used to measure electron properties in plasmas. The method involves directing a laser beam into the plasma, where the photons scatter off the free electrons. The scattered spectrum allows for the inference of key electron properties, such as density, velocity distribution, and temperature, if we assume that the velocity distribution is Maxwellian. The noninvasive nature of LTS makes it particularly valuable for detailed studies of dynamic plasma behaviors in various applications. Recently, advances in hardware have enabled the necessary sensitivity for LTS to be applied to the low-temperature, low-density plasmas present in HETs [12]. This manuscript presents measurements of near-field electron properties with the HET in three different electrical configurations, body grounded, body floating, and body tied to cathode common. The axial electron number density and temperature profiles are compared. Additionally, power spectral density profiles of the thruster discharge current are also presented for each configuration.

III. Experimental Setup and Methodology

This section describes the vacuum facility in which the experiment was conducted, the H9 HET setup and operation, the LTS diagnostic setup, and the theory used to infer the electron parameters of interest. The combined experimental

Downloaded by Georgia Institute of Technology (Georgia Tech) on January 17, 2025 | http://arc.aiaa.org | DOI: 10.2514/6.2025-1099

configuration allows for simultaneous investigation of thruster operation and plasma properties under controlled vacuum conditions.

A. Facility

The experiment was carried out in Vacuum Test Facility 2 (VTF-2) at Georgia Tech's High Power-Electric Propulsion Laboratory (HPEPL). VTF-2 measures 9.2 meters in length and 4.9 meters in diameter. The chamber is then evacuated to a moderate vacuum of approximately 10 mTorr measured with an Agilent Varian 531 Thermocouple Vacuum gauge. This rough vacuum was achieved through one 3800 CFM blower and one 495 CFM rotary-vane pump. To reach high vacuum, the facility utilizes 10 LN_2-cooled CVI TMI reentrant cryopumps that provide a pumping speed of ~400,000 l/s on krypton. The pressure in the high-vacuum phase of operation is measured in three locations: two internal and one external mounted on a chamber flange. All three locations employ an Agilent Bayard-Alpert 571 hot-filament ion gauges. Averaging over the three measurements provides a base pressure of 9.1×10^{-8} Torr and an operational pressure of 7.7×10^{-6} Torr-Kr at a krypton anode flow rate of 230 sccm (14.37 mg/s) during this experiment.

B. Hall Effect Thruster and Operating Conditions

The experiment was performed using the H9 HET. The H9 is a 9-kW class magnetically-shielded HET developed by the Jet Propulsion Laboratory in collaboration with the University of Michigan and the Air Force Research Laboratory [13]. The H9 employs a centrally mounted lanthanum hexaboride (LaB_6) hollow cathode, a boron nitride discharge channel, and graphite inner and outer front pole covers. The nominal operating conditions for this thruster are 15 A at 9 kW, 20 A at 6 kW, and 15 A at 4.5 kW. The thruster performance on krypton at the 6-kW operating condition was documented by [14] and can be found in Table 1.

Table 1: Thruster Performance

Operating Condition (kW)	Thrust (mN)	I_{sp} (s)	Anode Efficiency	Background Pressure (μTorr-Kr)
6	250	2000	0.56	5.93

The H9 anode and cathode were supplied with a mass flow of krypton with a purity of 99.999% measured by MKS GE50A mass flow controllers (MFCs). The MFCs were calibrated at the test article using a MesaLabs DryCal 800-10 volumetric flow meter, and a linear fit was generated between the commanded and measured flow rates.

The thruster is powered by multiple power supplies. The thruster discharge power is supplied by a Magna-Power TSA800-54 power supply in series with a 95-μF capacitor and 1.3-Ω resistor to prevent discharge current oscillations of above 1.4 kHz. The cathode heater, cathode keeper, and inner and outer magnet coils are powered by TDK-Lambda GEN60-25, GEN600-2.6, GEN40-38, and GEN80-42 power supplies, respectively. Time-resolved thruster telemetry is measured with a Teledyne LeCroy HDO6104 oscilloscope with a 1 MS/s sampling rate. Thruster telemetry recorded includes time-resolved measurements of the discharge current, discharge voltage, thruster body-to-ground voltage, and the cathode body-to-ground voltage. The discharge voltage is measured with a Powertek DP25 differential voltage probe rated up to 25 MHz. The discharge current is measured on the anode electrical line in the control room using a Teledyne Lecroy CP150 current clamp. Additionally, the oscilloscope records the discharge current data for the generation of PSD plots of the three electrical configurations.

The thruster is run at the same operating condition in all three electrical configurations. The thruster is run at one of the nominal H9 operating conditions of 6 kW with a discharge voltage of 300 V, a discharge current of 20 A, and a magnetic field 87.5% of the nominal magnetic field setting [14]. The anode flow rate was 229.6 ± 1.89 sccm-Kr (14.35 mg/s) with a cathode flow rate of 20.17 ± 0.45 sccm-Kr (1.26 mg/s). The discharge peak-to-peak values for the floating, grounded, and tied configurations were 17.10 A, 9.70 A, and 15.92 A, respectively.

The electrical configurations are varied at the breakout box in the control room. Figure 1**Error! Reference source not found.** a, b, and c show the associated circuit diagrams for the floating thruster body, grounded thruster body, and cathode-tied thruster body, respectively. The floating thruster body configuration, further referred to as the "floating configuration," is where the thruster body is electrically isolated from the conducting vacuum chamber and floats at

Downloaded by Georgia Institute of Technology (Georgia Tech) on January 17, 2025 | http://arc.aiaa.org | DOI: 10.2514/6.2025-1099

some potential relative to ground. The grounded thruster body configuration, further referred to as the “grounded configuration,” is where the thruster is electrically tied to the vacuum chamber which is at electrical ground. The cathode-tied thruster body configuration, further referred to as the “tied configuration”, is where the thruster body is electrically tied to cathode common.

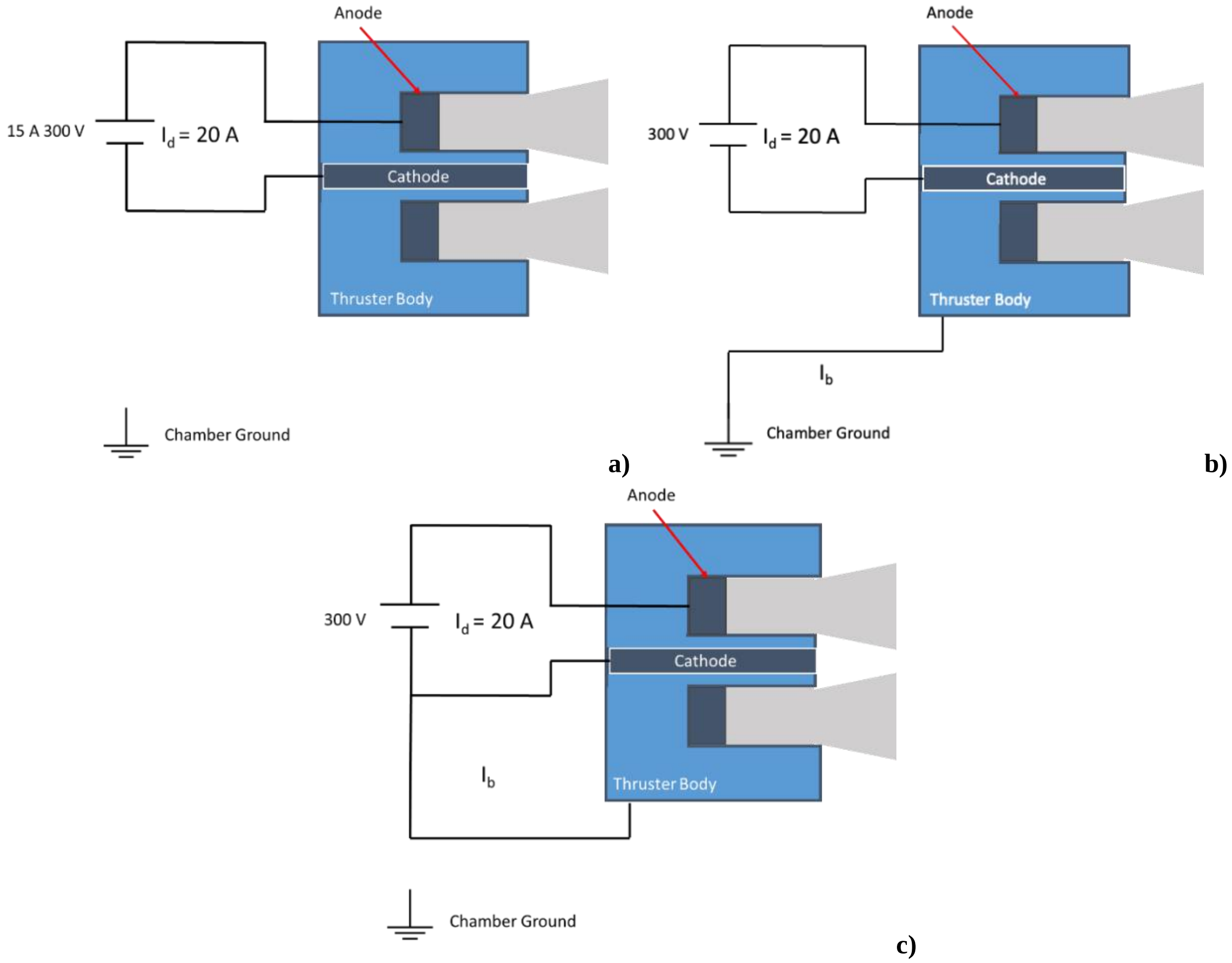

Figure 1: Circuits for each of the electrical configurations: a) floating, b) grounded, c) cathode-tied

To produce the spatially resolved electron properties in the near field of the thruster, the H9 was translated relative to the stationary LTS interrogation beam and collection optics using two Parker 4062000XR motion stages with ± 8 μm positional accuracy. Figure 2 shows the stages that enable probing of the near field of the thruster in the axial (z) and radial (r) directions.

Downloaded by Georgia Institute of Technology (Georgia Tech) on January 17, 2025 | http://arc.aiaa.org | DOI: 10.2514/6.2025-1099

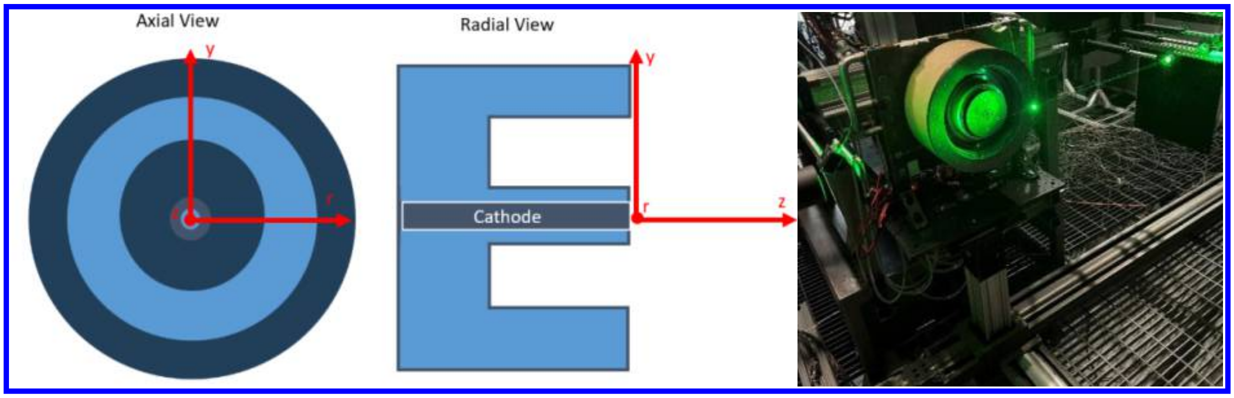

Figure 2: Measurement coordinate system and H9 on motion stages

C. Laser Thomson Scattering System

As previously mentioned, LTS in low-density plasmas involves laser photons scattering off free electrons in the plasma, collecting that scattered light, and performing spectral analysis that enables the inference of electron properties. The LTS system design is depicted in Figure 3 and is described in detail in Ref. [15]. To calibrate the LTS diagnostic absolute electron number-density measurements, a laser rotational Raman scattering (LRS) measurement was taken at 5 Torr. This pressure was measured with a Kurt J. Lesker XCG-BT-FB-1 capacitance manometer chosen for its accuracy of ± 0.5%.

An Amplitude DLS Powerlite 9010 injection-seeded Nd:YAG laser, operating at the second harmonic wavelength of 532 nm, delivered a beam diameter of 9 mm. The laser pulse duration ranged between 5 and 8 ns, with a maximum energy output of 1.15 J per pulse with a 10 Hz repetition rate. However, due to internal misalignments with the laser, the maximum laser output is approximately 670 mJ/pulse. The optical beam path depicted in Figure 3 is as follows: the beam exits the laser, intersects a mirror, turns into a beam expander assembly, and then into a half-wave plate and polarizing beam splitter cube so that the laser energy can be modulated without changing the timing settings internal to the laser. From there, the laser energy is measured using a power meter on a flip mount, allowing quick, unobtrusive energy measurements between laser Thomson scattering acquisitions. The energy is averaged over the 2.5-minute acquisition duration and measured by a Gentec UP52N-50S-QED-D0 power meter, which corresponds to PM in Figure 3. The beam turns again and goes through another half-wave plate that determines the final polarity of the beam before it enters the vacuum chamber through the periscope and Brewster window. The beam waist of about 100 μm intersects with the observation volume 2 mm downstream of the thruster face through a 600-mm focal length lens inside the chamber. The scattered light is collected and transmitted through two custom Thorlabs FG200LEA-FBUNDLE fiber bundles that contain seven 200-μm FG200LEA multimode fibers. The two fiber bundles are connected in series through a flange, allowing the collected light at the thruster to be relayed out of the chamber and into the external collection system. The light relayed through the bundles is spectrally filtered through two Optigrate OD-4 Bragg Notch Filters (BNFs) and then delivered to the spectrograph. The spectrograph consists of a Princeton Instruments ISOPLANE-320A spectrometer and a PM4-1024i-HB-FG-18-P46 PIMAX4 camera [16]. The collection fibers are delicately aligned to account for the chamber compression from the atmosphere to high vacuum. To enable this, the internal fiber bundle is placed on three motorized stages. Fine alignments at the axial location nearest to the cathode centerline are also made between each measurement to ensure that the maximum signal at the start of the experiment can be recovered throughout. For further details on the optical system design and alignment, refer to Ref. [15].

Downloaded by Georgia Institute of Technology (Georgia Tech) on January 17, 2025 | http://arc.aiaa.org | DOI: 10.2514/6.2025-1099

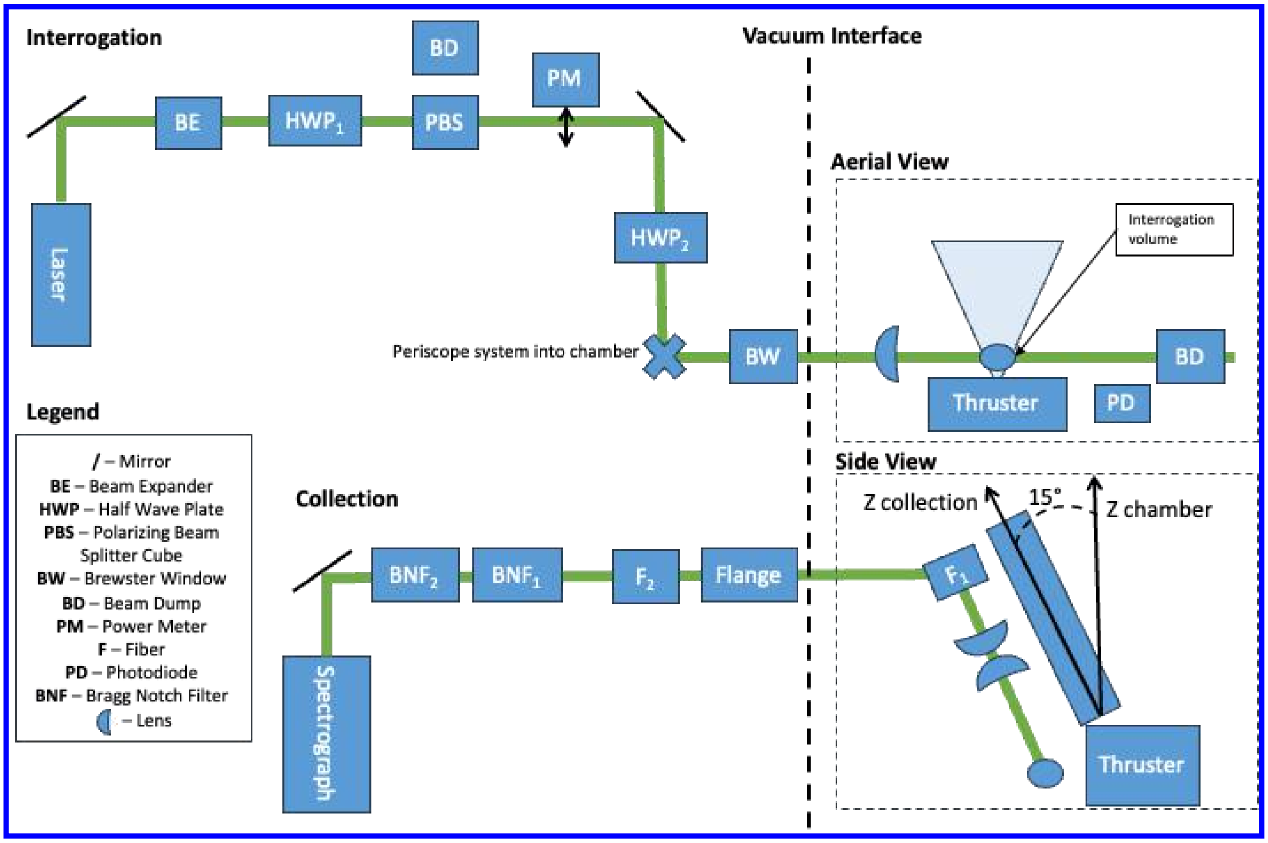

Figure 3: Master optical diagram for the interrogation, collection, and detection systems

IV. Theory

This section describes the data processing theory and procedures associated with extracting electron properties using scattered spectra from laser Raman and Thomson scattering diagnostics. The following sections serve as an overview of the equations employed for the data analysis. For detailed derivations and fitting procedures, see Ref. [15].

A. Calibration Coefficient Estimation using LRS Spectra

Before the LTS spectra can be analyzed for the estimation of electron properties, more specifically, the absolute electron number density, an intensity calibration using laser Raman scattering (LRS) is necessary to determine the transmission efficiency of the detection branch. LRS is the inelastic scattering of monochromatic laser light by polyatomic molecules resulting in a shift in energy corresponding to the internal energy modes of the molecule. This calibration is conducted by comparing the calculated synthetic spectra of the rotational Raman spectra of air at representative pressures with the experimental measurements. Agreement between the two provides for a more accurate estimation of the calibration coefficient. The expression corresponding to the synthetic Raman spectra of air assumed to comprise 79% nitrogen and 21% oxygen is given by **1**, and a detailed derivation can be found in Ref. [15].

$$P_\lambda^R(x^R,\theta^R) = \eta\frac{\lambda_i}{hc}\Delta\Omega L E_i n_g(T_g,p_g)\times\left[\gamma_{N_2}\left[\sum_J \frac{\partial\sigma^R}{\partial\Omega_{J'}}\right]_{N_2} + \gamma_{O_2}\left[\sum_J \frac{\partial\sigma^R}{\partial\Omega_{J'}}\right]_{O_2}\right] S_\lambda^R(\lambda_{J'},\tau) \qquad \text{Equation 1}$$

$$\gamma_{N_2} = 0.79 \text{ and } \gamma_{O_2} = 0.21$$

Where P_λ^R is the expected Raman signal in photon counts per nm. The parameters extracted and fitted to are $x^R = [T_g, \tau, \eta, \lambda_i]$. The $S_\lambda^R(\lambda_{J'},\tau)$ term is the spectral redistribution function and is given by **2** where it is assumed that the only relevant source of spectral redistribution is due to the instrument function as Doppler and pressure broadening are negligible [15].

Downloaded by Georgia Institute of Technology (Georgia Tech) on January 17, 2025 | http://arc.aiaa.org | DOI: 10.2514/6.2025-1099

$$S^R\left(\lambda_{J'},\tau\right) = \frac{1}{\sqrt{2\pi}\sigma_{IF}(\tau)} exp\left[-\frac{1}{2}\left(\frac{\lambda_i-\lambda_{J'}}{\sigma_{IF}(\tau)}\right)^2\right] \tag{Equation 2}$$

Where the Gaussian instrument function width σ_{IF} is a function of the full-width half maximum, τ and is given by

$$\sigma_{IF}(\tau) = \frac{\tau}{2\sqrt{2log\,(2)}} \tag{Equation 3}$$

The $\sum_J \frac{\partial\sigma^{\boldsymbol{R}}}{\partial\Omega_{J'}}$ terms are the rotational Raman scattering cross sections for each of the gases and is comprised of the sum of the Stokes and anti-Stokes cross sections, $\frac{\partial\sigma^{\boldsymbol{R}}}{\partial\Omega} = \sum_J \frac{\partial\sigma^{\boldsymbol{R}}}{\partial\Omega_{Stokes}} + \sum_J \frac{\partial\sigma^{\boldsymbol{R}}}{\partial\Omega_{Santi-tokes}}$. In Raman scattering, re-emitted or scattered photons can either be higher (anti-Stokes) or lower (Stokes) energy than the incident photon. The rotational selection rules dictate which rotational transitions are allowed when the molecule absorbs or emits a photon. For diatomic molecules, only J to $J \pm 2$ transitions are authorized [17]. The Stokes and anti-Stokes cross-sections are functions of the perpendicular scattering cross-section, $\frac{\partial\sigma^{\perp}}{\partial\Omega_{J'}}$, through the following expression [15],

$$\frac{\partial\sigma}{\partial\Omega_{J'}} = \frac{n_J}{n_g}\{(1-\rho)cos^2(\zeta)[1-cos^2(\theta_{kio})sin^2(\theta_{eiz})] + \rho\}\frac{\partial\sigma^{\perp}}{\partial\Omega_{J'}} \tag{Equation 4}$$

Where the perpendicular scattering cross section is given by [15],

$$\frac{\partial\sigma^{\perp}}{\partial\Omega_{J'}} = \frac{64\pi^4\gamma^2 b_{J\prime}}{45\ \epsilon_o^2\lambda_{J\prime}^4} \tag{Equation 5}$$

$\frac{n_J}{n_g}$ is the population fraction and is given by [15],

$$\frac{n_J}{n_g} = \frac{1}{Q_g} g_j(2J+1)exp\left[\frac{\epsilon_J(J)}{k_B T_g}\right] \tag{Equation 6}$$

Where Q_g is the rotational partition function, ϵ_J is the rotational energy mode, p_g is the pressure of the gas via the ideal gas law, $b_{J\prime}$ is the Placzek-Teller coefficient, and λ_j is the scattered wavelengths [15],

$$Q_g = \frac{(2I_g+1)^2 k_B T_g}{2B_g hc} \tag{Equation 7}$$

$$\epsilon_J(J) = hc[B_g J(J+1) - D_g J^2(J+1)^2] \tag{Equation 8}$$

$$p_g = n_g k_B T_g \tag{Equation 9}$$

$$b_{J\prime} = \frac{3(2J+1\pm1)(2J+1\pm3)}{8(2J+1)(2J+1\pm2)} \tag{Equation 10}$$

$$\lambda_{J'}(J) = \lambda_i \pm {\lambda_i}^2 B_g(4J+2\pm4) \tag{Equation 11}$$

Downloaded by Georgia Institute of Technology (Georgia Tech) on January 17, 2025 | http://arc.aiaa.org | DOI: 10.2514/6.2025-1099

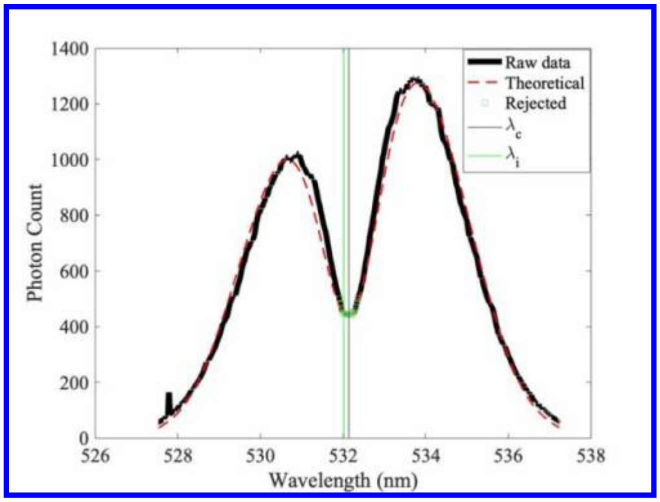

Figure 4: Example of a Raman scattering spectrum on air used for calibration

Figure 4: Example of a Raman scattering spectrum on air used for calibration shows an example of a Raman scattering spectrum. The black "+" symbols represent the experimental data, while the dashed red line corresponds to the expression shown in **1** to which the experimental Raman data is fit. The green boxes illustrate the rejection measurements that are usually intense and centered around the interrogation laser wavelength as they are affected by light redistribution at the stray light peak [12]. However, as is evident in the plot, the BNF filtering effectively attenuated stray light at 532 nm while permitting the Stokes and anti-Stokes transitions to be clearly distinguishable.

B. Electron Property Estimation using LTS Spectra

To estimate the electron properties from LTS spectra, the experimental data is fit to the expression Equation 12 for the total Thomson scattered spectrum power, P_λ^T, that is a function of the wavelength of the scattered light. The scattering spectrum's redistribution is primarily influenced by wavelength shifts due to the relative motion or velocity of the scattering electrons with respect to the reference or incident wavelength. The shape of the distribution, governed by the Thomson spectral redistribution function, denoted by $S_k(\lambda)$, is related to the electron velocity distribution function, which is assumed to be Maxwellian if the electrons are in thermal equilibrium [15].

$$\mathrm{P_\lambda^T(x^T, \theta^T) = \eta \frac{\lambda_i}{hc} \Delta\Omega L E_i n_e \frac{\partial\sigma^T}{\partial\Omega} S_{k,\lambda}^T(x^T, \lambda_i)} \qquad \text{Equation 12}$$

Where the fitted to and parameters extracted are $x^T = [T_e, n_e, v_d]$, and $\theta^T = [\eta, \lambda_i]$. The spectral redistribution function for a Maxwellian plasma is given by,

$$S_{k,\lambda}^T = \frac{1}{\sqrt{2\pi} k_\sigma \sigma_T} \exp\left[-\frac{1}{2}\left(\frac{\omega_i - \omega - k_\sigma v_d}{k_\sigma \sigma_T}\right)^2\right] \qquad \text{Equation 13}$$

The error of each of the extracted parameters is estimated from the 95% confidence bounds obtained from the Curve Fitting Toolbox in MATLAB.

Each acquisition was comprised of some combination of frame and on-ccd accumulations that totaled 1500 shots. The grounded configuration scans were acquired with 30 on-ccd accumulations and 50 frames, while the tied and floating configurations were acquired with 25 on-ccd accumulations and 60 frames. The motivation here was to minimize the noise on the detector relative to the raw Thomson signal. To isolate the scattered spectrum due only to Thomson scattering, four spectra were acquired at each axial location. The first is the raw spectra ("A") with both the laser and thruster on. The second is the emission spectra ("B") acquired with the laser off while the thruster is on to capture the plasma emission from the thruster. The third is the reflection spectra ("C") acquired with the laser on while the thruster is off to capture the stray light reflections of the interrogation beam off reflective surfaces in the chamber. Finally, the background ("D") with both the laser and thruster off is used to capture and subtract the detector noise. The resultant Thomson signal is given by,

$$\text{Resultant Thomson Signal} = A - (B + C - D)) \qquad \text{Equation 14}$$

Downloaded by Georgia Institute of Technology (Georgia Tech) on January 17, 2025 | http://arc.aiaa.org | DOI: 10.2514/6.2025-1099

See Figure 5 for all four spectra and the resultant Thomson signal on which all measurements were performed. The green boxes in Figure 5a) represent the width of the rejected region, which was estimated as a fixed multiple of the inferred FWHM of the distribution and varied arbitrarily between data sets. Figure 5b shows an example of the raw, emission, reflection, and background spectra that are input into Equation **14** to give the spectra used for analysis, denoted as the "Thomson" spectra.

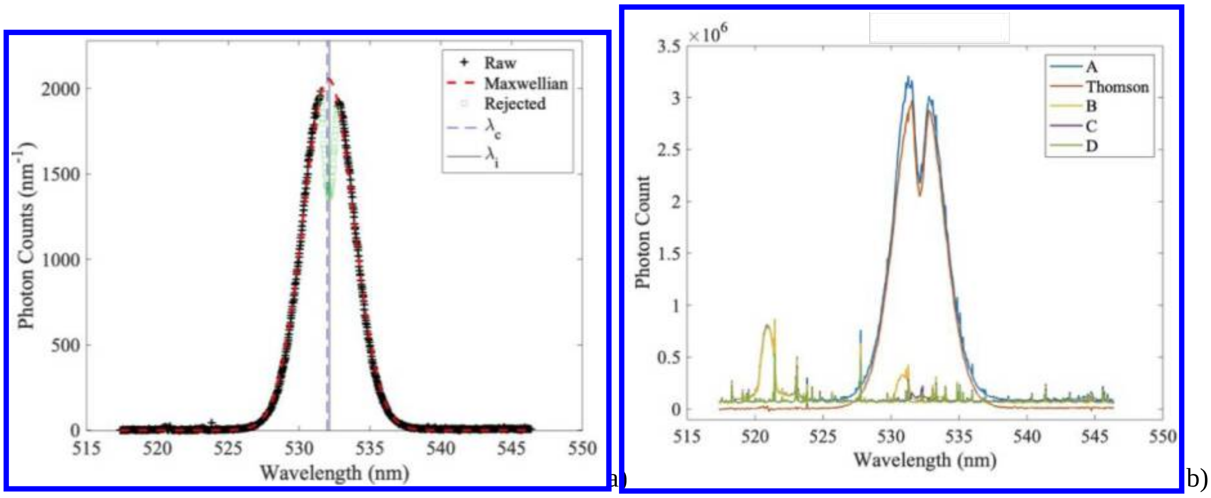

Figure 5: a) Example of processed LTS spectra, b) Example of raw spectra A, B, C, and D, that were input into Equation 14 to obtain the resultant Thomson spectra

V. Experimental Results and Discussion

The primary focus of this study is the axial characterization of the electron number density and temperature of the cathode plasma with the thruster body in three electrical configurations and, thus, potentials. A secondary objective is to characterize how the power spectral density distribution changes in the different electrical configurations. The goal is to understand the impact of the electrical configurations on the near-field plasma characteristics.

A. Electron Property Comparisons

1. *Electron Number Density*

Figure 6 a shows the electron number density, n_e, as a function of axial position for all three electrical configurations. As expected, the electron number density exponentially decays as the axial distance downstream of the cathode exit increases [15]. All three electrical configurations have a maximum electron density of an order of magnitude of 1×10^{19} m^{-3}, which is consistent with expected values at the cathode centerline based on measurements reported in other literature. In Ref. [15], the electron number density at the cathode centerline of the same cathode operating at 25 A on krypton was 1×10^{18} m^{-3} at the closest axial location of 2 mm from the cathode face. This study employed a wide diameter external anode, which would result in a more diffuse, and thus less dense, cathode plasma, and thus may explain the order of magnitude difference with our results. Neutral density simulation results for the HERMeS thruster operating at nominal conditions in [18] showed that the neutral density stays above 1×10^{19} m^{-3} up to 15 mm downstream of the cathode centerline, whereas the measurements in this study drop an order of magnitude ~ 5 mm downstream. This discrepancy between these measurements is likely attributed to the fact that the neutral flow simulation does not account for various plasma effects present in the experimental environment, *e.g.*, charge exchange collisions and ionization.

The electron density exhibits a significant decrease of approximately two orders of magnitude over the 17 mm axial distance, consistently across all electrical configurations before converging. This convergence in the far-field suggests that electron density measurements taken far from the thruster face may not effectively differentiate between electrical configurations. Beyond 2 mm downstream of the cathode face, the cathode-tied configuration maintains the highest

Downloaded by Georgia Institute of Technology (Georgia Tech) on January 17, 2025 | http://arc.aiaa.org | DOI: 10.2514/6.2025-1099

electron density among the three configurations. This phenomenon can be attributed to the thruster chassis being electrically tied to the cathode common, thus functioning as the plasma's negative electrode. The central mounting of the cathode combined with the conducting pole covers of the H9 thruster creates a specific plasma-surface interaction geometry, where the inner front pole cover, being the nearest conducting surface to the cathode exit, has some influence on the cathode plasma. The thruster face's direct contact with the plasma leads to stronger sheath formation compared to the circumferential thruster body components. These effects would likely be minimal with an externally mounted cathode configuration, as thruster body potential changes would have limited influence on local cathode plasma density.

The grounded configuration exhibits lower electron density magnitudes compared to other configurations. Substantial electron collection occurs at the thruster body, with measurements from Peterson et al. showing up to 13% of discharge current can be collected by the thruster. The conducting and grounded inner front pole cover is likely to provide a preferential electron pathway, creating a low-resistance path to the vacuum chamber. This pathway enables electron recombination with plume ions at chamber walls, as McDonald reported [8]. Due to the presence of these low-resistance, artificial recombination pathways, electrons may be collected before significant downstream propagation into the discharge plasma.

In the floating configuration, electron collection occurs primarily when electron thermal energy is sufficient to overcome the strong repulsive electric potential of the plasma sheath present on the thruster body as it tries to maintain a zero net charge flux. In this experiment, the thruster body voltage was approximately 20 V below ground in the floating configuration compared to ~15 V in the tied configuration. This configuration typically results in reduced electron collection by the thruster body compared to other configurations, as electrons would need to possess electron energies more than the very negative floating potentials HET usually float to when in a floating configuration. Similar, yet more negative values of floating thruster body potential at a discharge voltage of 300 V were also measured for a 2-kW magnetically-shielded HET at -22 V [19] and the H6 HET at -33.2 V [8].

2. *Electron Temperature*

The electron temperature trends depicted in Figure 6b shows a temperature increase from ~2-4 eV as the axial downstream distance is increased from 2 mm to 17 mm. The most reported electron temperature in the inner front pole region is about 4 eV [20, 21]. This linear relationship is consistent with trends shown in standalone cathode discharges and is typically attributed to the expansion of the plasma toward an external anode [15]. The cathode plasma does expand into the discharge plasma, however, less so than it would in a standalone, external anode configuration, which explains the difference. The floating configuration having the highest T_e of the electrical configurations aligns with the idea that because of the low floating voltage, the sheath potential on the body in the inner front pole region is the highest relative to the other electrical configurations. This would necessitate repelled electrons to have higher kinetic energy as they are accelerated by the strongest sheath potential of the three electrical configurations. This conclusion is validated by the fact that the electron temperature comparison of the three electrical configurations tracks with what the expected sheath potential on the thruster body should be. Estimating this value based on just the measured thruster body-to-ground voltage shows the same trend, with the floating configuration measuring the highest at -18.8 V, the tied configuration at -14.9 V, and the grounded configuration at 0 V.

The potential difference across the sheath (φ_f) is dependent on the local electron temperature and is equal to $\varphi_f = \frac{kT_e}{e}\ln\left(\sqrt{\frac{2m_i}{\pi m_e}}\right)$, where $\frac{kT_e}{e}$ is the electron temperature in eV and $\frac{m_i}{m_e}$ is the ion-to-electron mass ratio. In the case of krypton propellant, the floating potential is $\sim 5.75\,\frac{kT_e}{e}$. The electron temperature near the inner front pole region can be estimated by leveraging the convergence behavior of electron temperature profiles. Recent spatially resolved measurements [15] demonstrated that axial profiles at radial locations $r = 0$ and 2 mm converge at $z = 6$ mm, suggesting minimal radial variation in electron temperature beyond this distance. Given that the inner front pole is the nearest conducting surface to the cathode face, it is reasonable to expect that the electron temperature profile downstream of the inner front pole cover would similarly converge with the cathode centerline profile at the maximum measured axial distance of 17 mm. Based on this assumption, the estimated T_e of 3-4 eV at the inner front pole yields a sheath potential, φ_f, of approximately 20.1 V, which corresponds well with the measured thruster body-to-ground voltage of ~19 V in the floating configuration.

Downloaded by Georgia Institute of Technology (Georgia Tech) on January 17, 2025 | http://arc.aiaa.org | DOI: 10.2514/6.2025-1099

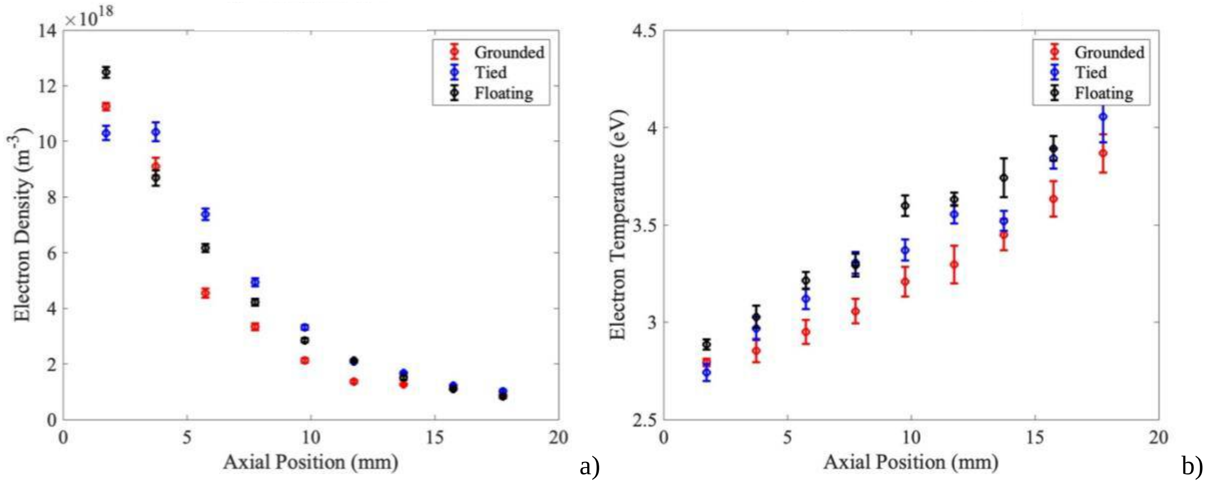

Figure 6: a) Electron number density as a function of axial position in the grounded, cathode-tied, and floating configurations inferred from the LTS spectrum as a function of distance from the cathode taken at a radial location of cathode centerline. b) Electron temperature as a function of axial position in the grounded, cathode-tied, and floating configurations inferred from the LTS spectrum as a function of distance from the cathode taken at a radial location of the cathode centerline.

B. Power Spectral Density Comparison

Peaks in the discharge current are attributed to the depletion of neutral populations in the discharge chamber as a result of ionization. The frequency content in the time-resolved discharge current gives information about the frequency at which that process is happening. The dominant or peak frequency is called the breathing mode [10] and can be found by performing power spectral density (PSD) analysis on the discharge current. PSD plots compared across the electrical configurations, as shown in Figure 7a, reveal an increase in the frequency. The frequency shift was not expected as similar PSD comparisons made for the HERMeS thruster in three electrical configurations from Peterson *et al*. show the opposite trend, with the main frequency increasing from the grounded to floating configurations. Both thrusters are magnetically shielded and in a comparable power class; however, the discrepancy is likely because the relationship between the thruster body potential and breathing mode frequency cannot be assumed to be linear, as shown in Walker *et al*. [22]. The plots therein depict the relationship for the T-140, with an externally-mounted cathode, and show more of a parabolic relationship between the thruster body potential and breathing mode frequency. Because of this, it is assumed that this relationship would need to be characterized for each individual thruster as it is likely dependent on the cathode position, pole cover material, and operating condition. To determine whether the same trend was present at higher discharge power levels, a comparative PSD plot was generated at the nominal 600 V, 9-kW operating condition as well. However, only the floating and tied configurations could be assessed. Without the grounded configuration, it is difficult to definitively say the trends match. The floating main frequency is still less than that of the tied configuration, which is true for both power levels.

Downloaded by Georgia Institute of Technology (Georgia Tech) on January 17, 2025 | http://arc.aiaa.org | DOI: 10.2514/6.2025-1099

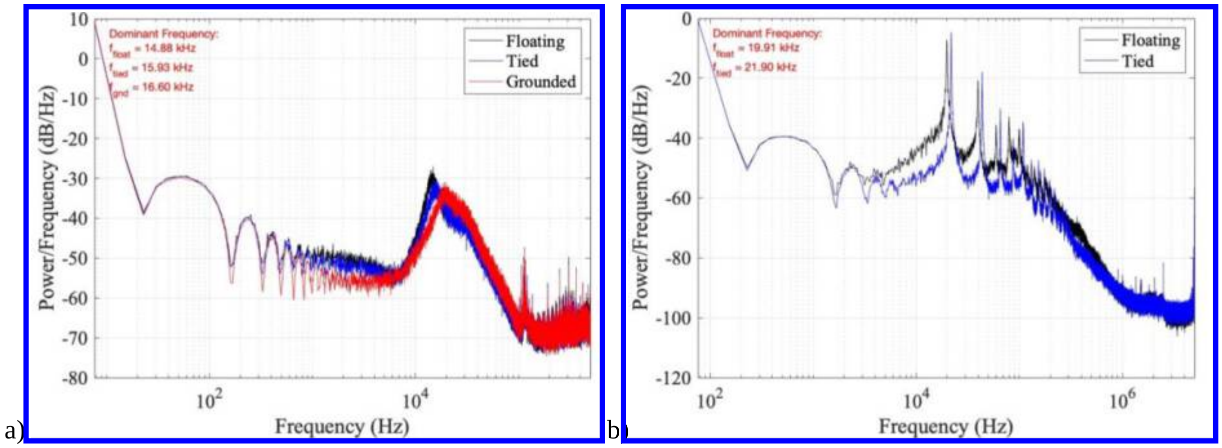

Figure 7: PSD plot as a function of electrical configuration at the a) 6-kW, 300 V and b) 9-kW, 600 V operation conditions.

Because the PSD plots of the various electrical configurations show a slight shift in primary oscillation frequency and amplitude, also found to be true in [6], there is a possibility that the acceleration and ionization region lengths are varying due to the relation in Equation 15 [10].

$$L_{\text{ion/accel}} = \frac{\sqrt{V_{ion}V_n}}{2\pi f_i} \qquad \text{Equation 15}$$

Considering that magnetic shielding already shifts the acceleration region downstream toward the exit plane compared to unshielded HETs, there is more opportunity for cathode plume electrons to intersect and influence said region. It was also seen that these differences in oscillation characteristics are more drastic at higher power conditions; Figure 7b shows more dramatic changes in near-field plasma dynamics as a function of thruster electrical configuration at higher power levels. According to this relationship and the data presented in Figure 7a, the floating configuration should have the longest acceleration region relative to the other configurations, and the grounded configuration should have the shortest. We postulate, especially in the case of magnetically shielded thrusters, that the electrons repelled due to large negative thruster floating potentials are likely the reason for the downstream extension of the ionization front in this case. The strong electron repulsion is likely to make it more difficult for them to reach the ionization region [22]. Conversely, in the grounded configuration, the thruster body attracts electrons back toward its face, enabling them to enter the discharge chamber more readily.

C. Thruster Body Current

A natural approach for analyzing thruster body current collection is to model the electron and ion currents under the assumption of a Maxwellian electron population near the thruster surface. While direct measurements of thruster body current were not taken during this experiment, theoretical calculations can provide insight into current collection behavior as a function of body-to-cathode potential and electron temperature. Figure 8 shows the simulated net current into the thruster body inner front pole surface area as a function of body to cathode voltage.

Downloaded by Georgia Institute of Technology (Georgia Tech) on January 17, 2025 | http://arc.aiaa.org | DOI: 10.2514/6.2025-1099

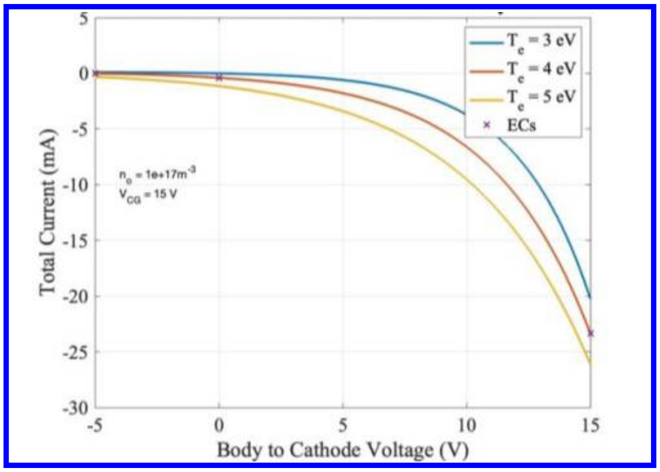

Figure 8: Simulated total current through thruster body as a function of body-to-cathode voltage for electron temperatures in the range of 3-5 eV.

The current collected by the thruster body was not measured during this experiment, but under the assumption that electrons near the thruster surface are Maxwellian, the electron current, I_e, into the thruster body through the inner front pole can be calculated using Equation 16,

$$I_e = A_s e\sqrt{\frac{kT_e}{m_i}}\ 0.606 n_o exp\left(-\frac{e\Delta\emptyset}{kT_e}\right) \qquad \text{Equation 16}$$

A_s is the surface area of the inner front pole, $\sqrt{\frac{8kT_e}{\pi m_e}}$ is the mean electron thermal velocity, n_o is the local plasma density, and $\Delta\phi$ is the sheath difference between the plasma potential and the thruster body potential. The local plasma density in front of the front pole is assumed to be 1 x 10^{17} m^{-3} based on simulations. The collected ion current, I_i, can be calculated with Equation 17,

$$I_i = A_s e\sqrt{\frac{kT_e}{m_i}}\ 0.606 n_o \qquad \text{Equation 17}$$

where $\sqrt{\frac{kT_e}{m_i}}$ is the ion Bohm velocity [22]. Using the convention that ion current is positive, and electron current is negative, the same approach to plotting the collected current to the witness plate applied by Walker *et al.* [22] is applied and shown in Figure 8. While the simulated collected current cannot be validated by measurements, the data for an electron temperature of 4 eV shows the switch in sheath polarity at the expected body-to-cathode voltage of 0 V. The simulated results lend further credence that at body voltages positive relative to the cathode potential, and especially when grounded, significant electron current is collected through the body, resulting in a reduced number of electrons capable of propagating downstream.

VI. Conclusion

This work characterizes the electron density and temperature downstream of the cathode centerline of the thruster in three electrical configurations: floating, tied, and grounded. The results show that in the tied configuration, electron number density is highest in the near field, while in the floating configuration, the electron temperature is the highest. Varying the electric potential on the thruster body provides the ability to manipulate plasma properties, and more specifically electron current pathways, in the near field of the cathode plasma and surrounding conducting thruster body components. It is postulated that the local electron current density downstream of the cathode is significantly influenced by the electrons collected by the thruster body when the sheaths on its plasma-facing surfaces are electron-attracting. The local electron temperature appears to change because of the magnitude of the potential drops across

Downloaded by Georgia Institute of Technology (Georgia Tech) on January 17, 2025 | http://arc.aiaa.org | DOI: 10.2514/6.2025-1099

the surface sheaths. The electron-repulsive sheaths are then able to impart kinetic energy by accelerating electrons that do not have enough energy to overcome these sheath potentials.

Additionally, this change in local plasma properties appears to connect to the global plasma environment via the frequency content present in the discharge current. PSD plots of the discharge current in each of the configurations show an increase in breathing mode frequency from floating to grounded configurations. The inverse relationship between the breathing mode frequency and the length of the acceleration region found by previous references is likely dependent on the availability of electrons, which is hypothesized to be greater in cases where electrons are attracted to the face of the thruster via its surface sheaths. These findings provide a path to understanding and characterizing how the electron dynamics change as a function of electrical configuration. However, not discussed or thoroughly considered in this work, is the influence of the magnetic field on these results. This provides some opportunities for future work. As the magnetic field downstream of the cathode is mostly axial, estimating perpendicular electron mobility in this region could provide a clearer picture of how electron pathways change as a result of thruster bias. Also, because the PSD plot differences are more prominent at higher discharge power conditions, future work may include measuring the length of the acceleration through axially resolved near field measurements of the T_e in the thruster channel in different electrical configurations to experimentally validate the numerical results.

Acknowledgments

This work was supported by a NASA Space Technology Graduate Research Opportunity (80NSSC20K1224).

References

---

[1] Smith, B. K., Nazario, M. L., & Cunningham, C. C., “Solar Electric Propulsion Vehicle Demonstration to Support Future Space Exploration Missions,” (2012). (No. E-18409).

[2] Goebel, D. M., Katz, I., and Mikellides, I. G., “Introduction; Hall Thrusters,” *Fundamentals of electric propulsion,* 1st ed., John Wiley & Sons, (2023), (pp. 7).

[3] Mikellides, I.G., Katz, I., Hofer, R.R. and Goebel, D.M., "Magnetic Shielding of a Laboratory Hall Thruster. I. Theory and Validation," *Journal of Applied Physics*, Vol. 115, No. 4, 2014, 043303. https://doi.org/10.1063/1.4862313

[4] Frieman, J. D., King, S. T., Walker, M. L. R., Khayms, V., and King, D., “Role of a Conducting Vacuum Chamber in the Hall Effect Thruster Electrical Circuit,” *Journal of Propulsion and Power*, Vol. 30, No. 6, 2014, pp. 1471–1479 https://doi.org/10.2514/1.B35308

[5] Walker, J.A., Langendorf, S.J., Walker, M.L., Khayms, V., King, D. and Pertson, P., “Electrical Facility Effects on Hall Current Thrusters: Electron Termination Pathway Manipulation,” *Journal of Propulsion and Power*, Vol. 32, No. 6, 2016, pp.1365-1377. https://doi.org/10.2514/1.B35904

[6] Peterson, P. Y., Kamhawi, H., Huang, W., Williams, G., Gilland, J. H., Yim, J., and Herman, D. A., “*Nasa's Hermes Hall Thruster Electrical Configuration Characterization.*”, AIAA Paper 2016-5027 (July, 2016). (pp. 5027).

[7] Koppel, C. R., & Estublier, D., “The SMART-1 Hall Effect Thruster Around the Moon: In Flight Experience,” IEPC 2005-119, (October, 2005).

[8] McDonald, M. S., “*Electron Transport in Hall thrusters*”, (Dissertation, University of Michigan), 2012.

[9] Kamhawi, H., Huang, W., Gilland, J. H., Haag, T. W., Mackey, J., Yim, J., ... & Herman, D., “Performance, Stability, and Plume Characterization of the HERMeS Thruster with Boron Nitride Silica Composite Discharge Channel,” IEPC 2017-392, (2017, October).

[10] Fife, J., Martinez-Sanchez, M., Szabo, J., Fife, J., Martinez-Sanchez, M., & Szabo, J., “A Numerical Study of Low-Frequency Discharge Oscillations in Hall Thrusters.”, AIAA Paper 1997-3052 (July, 1997).

[11] Hofer, R. R., Jorns, B. A., Katz, I., & Brophy, J. R. *U.S. Patent No. 10,480,493.* Washington, DC: U.S. Patent and Trademark Office. (2019)

[12] Vincent, B., *“Incoherent Thomson Scattering Investigations in Hall Thruster, Planar Magnetron and ECR Ion Source Plasmas.”* (Doctoral dissertation, Université d'Orléans). 2019.

[13] Hofer, R.R., Cusson, S.E., Lobbia, R.B. and Gallimore, A.D., “The H9 Magnetically Shielded Hall Thruster.” IEPC 2017-232 (October, 2017).

---

[14] Su, L. L., Vazsonyi, A. R., & Jorns, B. (2020)., "Performance of a 9-kW Magnetically-Shielded Hall Thruster with Krypton,", AIAA Paper 2022-3617, (August, 2022).

[15] Suazo Betancourt, J. L., Butler-Craig, N., Lopez-Uricoechea, J., Bak, J., Lee, D., Steinberg, A. M., Walker, M. L. R., "Thomson Scattering Measurements in the Krypton Plume of a Lanthanum Hexaboride Hollow Cathode in a Large Vacuum Test Facility," *Journal of Applied Physics*, Vol.135, No.8, 2024, pp. 083302. https://doi.org/10.1063/5.0180251

[16] Lopez-Uricoechea, J., Suazo Betancourt, J. L., Butler-Craig, N., & Walker, M. L. R., "Spatially Resolved Thomson Scattering Measurements of Electron Properties Across the Acceleration Region of a High-Power Magnetically Shielded Hall Effect Thruster," *Journal of Applied Physics*, Vol. 136, No. 11, 2024. https://doi.org/10.1063/5.0213928

[17] Bernath, Peter F., "*Spectra of atoms and molecules*.", Oxford University Press, (2020).

[18] Hall, S. J., Gray, T. G., Yim, J. T., Choi, M., Mooney, M. M., Sarver-Verhey, T. R., & Kamhawi, H., "The Effect of a Hall Thruster-like Magnetic Field on Operation of a 25-A Class Hollow Cathode*,",* IEPC 2019-300, (September, 2019).

[19] Watanabe, H., Cho, S., Kubota, K., Ito, G., Fuchigami, K., Uematsu, K., Tashiro, Y., Iihara, S. and Funaki, I., "Performance Evaluation of a Two-Kilowatt Magnetically Shielded Hall Thruster," *Journal of Propulsion and Power*, Vol. 36, No. 1., 2020, pp. 14-24. https://doi.org/10.2514/1.B37550

[20] Haas, J. and Gallimore, A., "An Investigation of Internal Ion Number Density and Electron Temperature Profiles in a Laboratory-Model Hall Thruster*,"* AIAA 2000-3422, (August, 2000).

[21] Herman, D., Shastry, R., Huang, W., Soulas, G., & Kamhawi, H., "Plasma Potential and Langmuir Probe Measurements in the Near-Field Plume of the NASA-300M Hall Thruster,", AIAA Paper 2012-4115, (July, 2012).

[22] Walker, J., Lev, D., Walker, M.L., Khayms, V. and King, D., "Electrical Characteristics of a Hall Effect Thruster Body in a Vacuum Facility Testing Environment," Journal of Electric Propulsion, Vol. 1, No. 1, 2022, article 18. https://doi.org/10.1007/s44205-022-00016-9

Downloaded by Georgia Institute of Technology (Georgia Tech) on January 17, 2025 | http://arc.aiaa.org | DOI: 10.2514/6.2025-1099